AGU100 ADVANCING EARTH AND SPACE SCIENCE

# JGR Planets

# Similarities and Differences of Global Dust Storms in MY 25, 28, and 34

**P. Wolkenberg[1], M. Giuranna[1], M. D. Smith[2], D. Grassi[1], and M. Amoroso[3]**

[1]Istituto di Astrofisica e Planetologia Spaziali-Istituto Nazionale di Astrofisica (IAPS-INAF), Rome, Italy, [2]NASA, Goddard Space Flight Center, Greenbelt, MD, USA, [3]Agenzia Spaziale Italiana (ASI), Sede di Matera, Italy

**Abstract** To better understand the dust cycle on Mars during years with planet-encircling dust storms, we analyze the last three events that took place in Mars Year (MY) 25, MY 28, and MY 34. Global dust storms that occurred in MY 25 and MY 34 (June 2018) were taking place during equinox, while the MY 28 storm had an onset after perihelion. Before the expansion phase of the MY 25 and MY 34 storms, we find similar regions (northern rim of Hellas, Arabia Terra, and Utopia Planitia) where dust is present. Possible precursor dust storms over Hellas and the southern polar cap edges were observed during MY 28 as a component of background dust activity. These features are not found in equinoctial dust storms on this scale. Dust during the MY 25 and MY 34 storms encircled the entire planet by the similar season ($L_s = 193°$). The MY 34 storm is characterized by a shorter decay phase compared to the events in MY 25 and MY 28. Dust opacity is correlated with atmospheric temperatures at 0.5 mbar and nighttime surface temperatures, while daytime surface temperatures are anticorrelated with dust opacity.

**Plain Language Summary** On Mars, one of the most variable atmospheric components is dust. We study it to better understand the cycle of its presence and absence in the Martian atmosphere. One of the particular phenomena of this cycle is the global dust storm that enshrouds the entire planet. Using data measured by two spectrometers, Thermal Infrared Emission Spectrometer onboard the Mars Global Surveyor and Planetary Fourier Spectrometer onboard the Mars Express orbiters, we investigate similarities and differences of the three most recent global dust storms that have occurred on Mars. We find similarities between the two global dust storms that took place in 2001 and 2018 (Mars Year [MY] 25 and 34). They encircled the entire planet in the equinox season. The storms in MY 25 and MY 28 dissipated over a very long timescale compared to the global dust storm of MY 34. Local dust storms in the northern rim of Hellas, Arabia Terra, and Utopia Planitia were observed before the onset of MY 25 and MY 34 global events.

## 1. Introduction

Global dust storms (GDSs) occur on Mars at irregular intervals, approximately every 3–5 Mars Years (MYs). They mostly originate in the southern hemisphere near perihelion from the combination of multiple local and regional dust lifting events (Haberle et al., 2017; Smith et al., 2002). However, GDSs have also been observed during the equinox seasons. Two seasons are recognized in the dust cycle through the whole Martian year. Elevated dust loadings mostly occur in the atmosphere from 130° to 360° of $L_s$ (Haberle et al., 2017). The clear season (nondusty, 0–130°) is described by low background level of 9-$\mu$m dust opacity between 0.1 and 0.2 (Smith, 2008). During this period, no large dust storms are observed with exception of regions near the retreating north polar cap edges (Smith, 2008). Observations of dust provide information on its location and time dependence in the Martian atmosphere and on the surface. During the locations and seasons with high dust loading, the thermal state of atmosphere and the atmospheric circulation are significantly affected (Cantor et al., 2001; Haberle et al., 2017).

Dust lifted into the atmosphere works as a positive feedback for some aspects of the atmospheric circulation (Cantor et al., 2001; Haberle et al., 1993). Haberle (1986) proposed an explanation for a mechanism for the origin of GDSs. Two regimes of Hadley circulation in the southern and northern hemispheres compete against each other during the dust storm season depending on the dust supply in each hemisphere. Dust can be transported from the southern hemisphere to the northern via the Hadley circulation. This circulation can be intensified by dust, and as a result, GDSs can develop, thereby suppressing the northern circulation built by midlatitude storm systems. On the other hand, in northern hemisphere, baroclinic wave activity

can raise dust into the atmosphere when there is sufficient dust on the surface. Northern dust haze can diminish the intensity of the Hadley circulation and in turn the surface stress in the southern hemisphere precluding the emergence of GDSs. In this paper, we analyze the last three GDSs, particularly the most recent one that occurred in MY 34 (Earth year 2018).

## 2. Data Sets

### 2.1. PFS Data Set

Data presented in this work (Wolkenberg et al., 2019) were retrieved from observations performed by the Planetary Fourier Spectrometer (PFS) onboard the Mars Express in the long-wavelength channel (LWC). They are part of a large data set composed of observations beginning in 2004 ($L_s = 330°$, MY 26) that continues to the present day (Giuranna et al., 2019). PFS measures radiation in its LWC that is dominated by the thermal emission by the planet. A complete description of PFS and its radiometric performance can be found in Formisano et al. (2005) and Giuranna et al. (2005a, 2005b). In the LWC, we observe some absorption features due to atmospheric constituents, mainly $CO_2$ and aerosols (dust and water ice). Using a retrieval algorithm (Grassi et al., 2005), we are able to derive information on the atmospheric parameters from these absorption bands. Temperature profiles are obtained from an analysis of radiation in the main $CO_2$ absorption band at 667 cm$^{-1}$ (15 μm). Total dust and water ice content in the vertical column are retrieved from wide absorption bands at 1,075 (9 μm) and 825 cm$^{-1}$ (12 μm), respectively. All these atmospheric parameters along with surface temperatures are retrieved simultaneously (Giuranna et al., 2019). In this work we use mostly daytime PFS measurements to be consistent with TES results.

### 2.2. TES Data Set

The Thermal Emission Spectrometer (TES) onboard the Mars Global Surveyor measured radiances in the spectral range from 200 to 1,600 cm$^{-1}$, which corresponds to LWC of PFS. A detailed characterization of the TES instrument is found in Christensen et al. (2001). Hence, the TES data set includes similar atmospheric parameters such as temperature profiles (Conrath et al., 2000) and dust and water ice aerosol optical depth (Bandfield & Smith, 2003; Smith, Bandfield, & Christensen, 2000; Smith, Pearl, et al., 2000). The same absorption bands as for PFS were used to retrieve atmospheric parameters. The surface temperatures are estimated from brightness temperatures at ~1,300 cm$^{-1}$ by using the improved algorithm presented by Smith (2004). Thus, a direct comparison of the TES and PFS retrieval data sets is possible (Wolkenberg et al., 2011). TES performed measurements at two local times (LTs) during day at 2 p.m. and during night at 2 a.m. We use the daytime observations.

## 3. Uncertainties of Dust Opacities

Uncertainties of dust opacities derived from TES observations come from two main sources. Random and systematic errors of instrument and its calibration are considered as a first source of uncertainty (e.g., Pankine, 2015, 2016). However, we use only daytime dust opacities when spectra have a sufficient contrast between surface and atmosphere. For those measurements, an improvement of calibration has no contribution to the shapes and relative strengths of the aerosols absorption features (Pankine, 2016). The other source takes into account errors in the retrieval algorithm. The final, total uncertainties of dust opacities are around 0.05 or 10% of the total optical depth (Smith, 2004). The PFS dust opacity uncertainties are based on the standard deviations of the final covariance matrix of atmospheric parameters to be retrieved (Wolkenberg et al., 2018). They found that the population of standard deviations of dust opacities were dependent on surface temperatures. Thus, this population was divided into two groups with surface temperatures less and larger than 220 K. For these two subsets, the standard deviations were estimated using histograms. For surface temperatures larger than 220 K, the typical standard deviations of dust opacities were 0.02 to 0.06, while for surface temperatures less than 220 K, the standard deviation was 0.11.

## 4. Basic Characteristics of Three GDSs

We consider the dusty season as the time interval from $L_s$ ~ 135° to 360° in each Martian year. Dust opacity can be elevated during different time periods of the dusty season. We distinguish a period of early-season and presolstice activity: $L_s$ ~ 135–236°, a period of solstitial activity near the South Pole: $L_s$ ~ 250–300°, and a
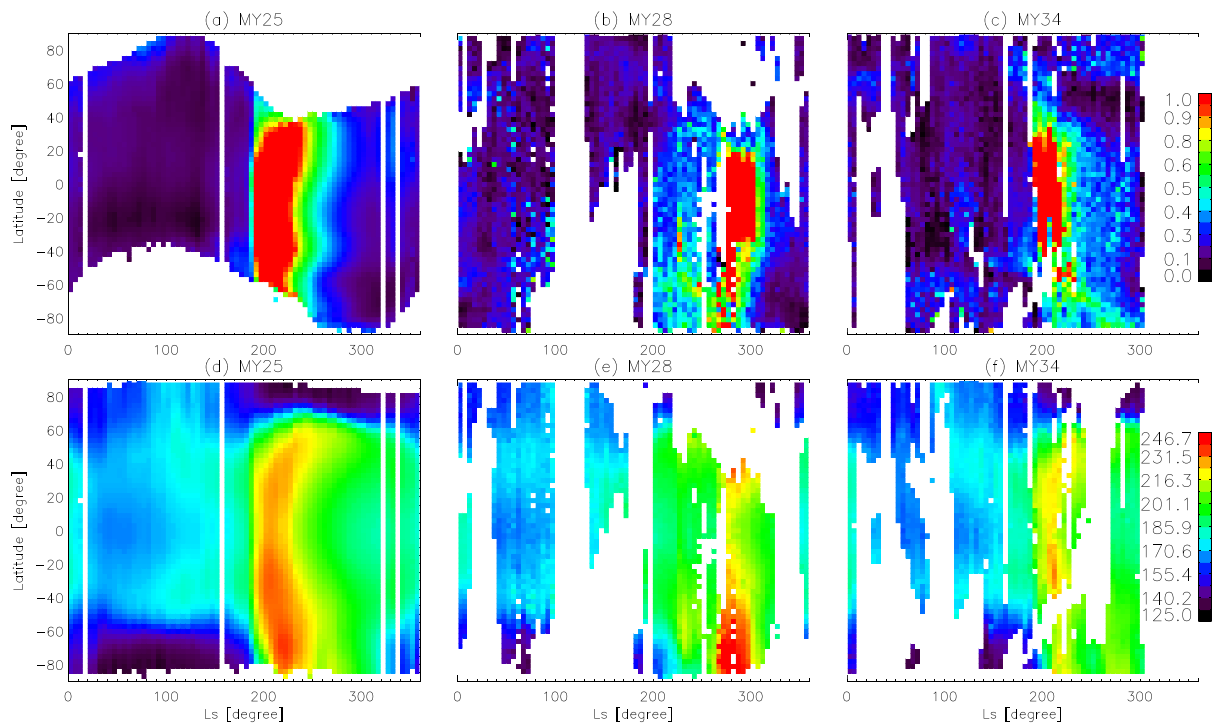
**Figure 1.** Zonally averaged dust opacities as a function of season and latitude for MY 25 (a), MY 28 (b), and MY 34 (c) scaled by surface pressure. Zonally averaged atmospheric temperatures at 0.5 mbar for MY 25 (d), MY 28 (e), and MY 34 (f). Data from MY 25 are retrieved from TES observations, while data from MY 28 and MY 34 are retrieved from PFS observations. PFS dust opacities are provided for all available LTs. Atmospheric temperatures at 0.5 mbar were retrieved from TES and PFS measurements performed at LT 14 and from 8 to 18 LT, respectively.

period of postsolstice activity: $L_s \sim 308$–$336°$ (Haberle et al., 2017). GDSs are events where enhanced dust loading encircles the entire planet. They take place during the dusty season with an irregular frequency averaging once every 3–6 MYs. In this work, we analyze the last three GDSs, which occurred in 2001 (MY 25), 2008 (MY 28), and 2018 (MY 34). The GDSs that occurred during MYs 25 and 34 began at $L_s \sim 185°$ during the period of early-season presolstice activity. On the other hand, the MY 28 dust storm began much later in season ($L_s \sim 265°$) during the period of solstitial activity. However, the MY 28 dust activity was not only constrained to near the South Pole. Elevated dust loading was distributed throughout the entire planet as for north as 40°N during this storm. The next section is dedicated to a presentation of the seasonal and spatial dust activity observed during the last three global storms.

## 5. Results

In this study we mainly focus on analysis of the column-integrated dust optical depths in three Martian years when GDSs occurred. The column-integrated dust optical depth is normalized to 610 Pa, according to the formula $\tau = 610 * \tau_0/P_{surf}$, where $\tau_0$ is the retrieved column-integrated dust optical depth and $P_{surf}$ is the surface pressure (Pa). For the purpose of characterizing the similarities and differences between the three GDSs, we use both the TES and PFS data sets.

### 5.1. Intercomparison of Zonal Mean Opacities and Temperatures for the Three GDSs

Figure 1 presents seasonal and latitudinal variability of zonally averaged dust opacities and atmospheric temperatures at 0.5 mbar (~25-km altitude) for the three specific Martian years 25, 28, and 34. Zonally averaged dust opacities have been binned by 5° in $L_s$ and by 3° in latitude. GDSs were observed during MY 25, MY 28, and MY 34 with dust opacities exceeding 1 at 1,075 cm$^{-1}$ over a large fraction of the planet. The GDS in MY 25 had the longest duration compared to other global storms considered here (Figure 1a). The MY 25 storm was apparently triggered from local dust storms (Figure 2a) that developed near the northwestern rim of the Hellas basin at $L_s = 177°$ (Strausberg et al., 2005). Probably, the local dust storms were induced by ice-cap
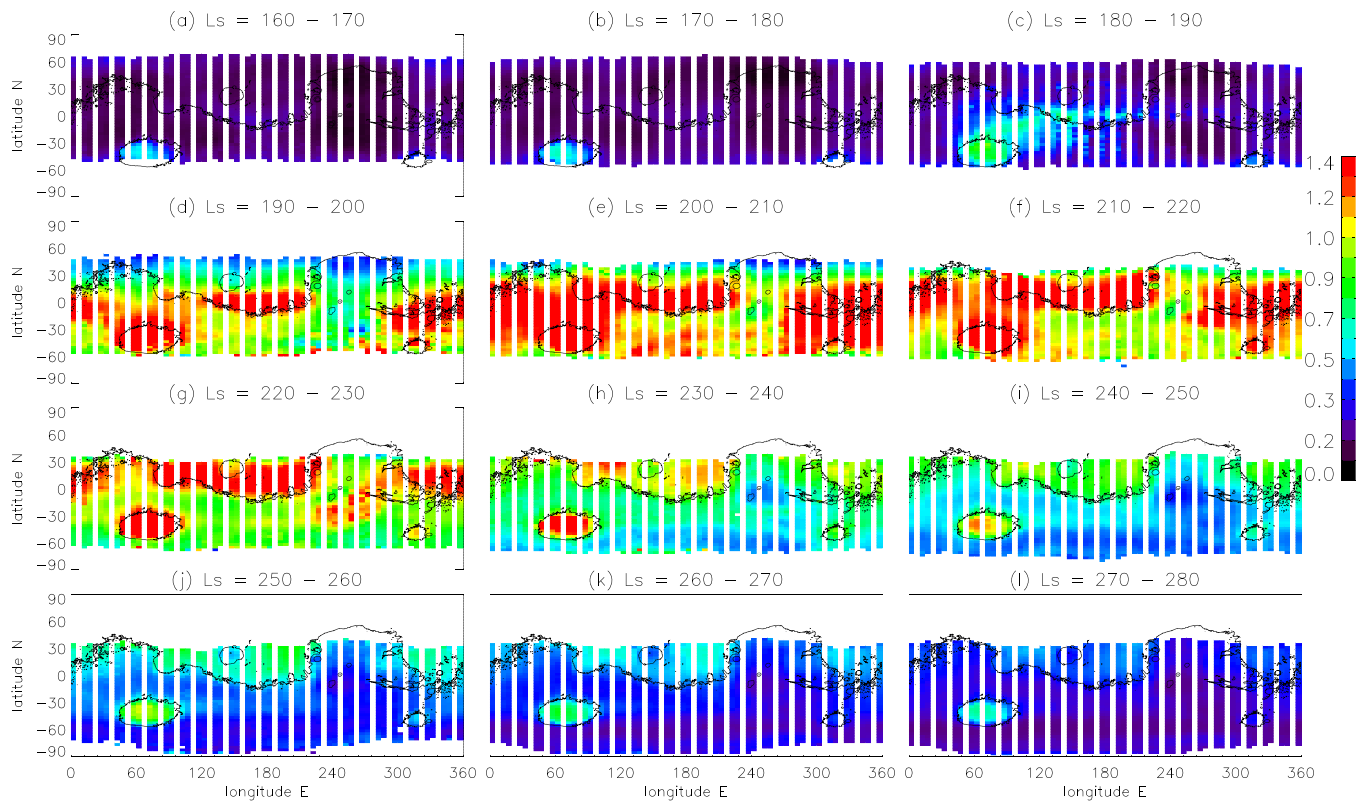
**Figure 2.** Spatial dust distributions (TES) from $L_s = 160°$ to $280°$ in MY 25 at 14 LT (local time), (a) $L_s = 160–170°$, (b) $L_s = 170–180°$, (c) $L_s = 180–190°$, (d) $L_s = 190–200°$, (e) $L_s = 200–210°$, (f) $L_s = 210–220°$, (g) $L_s = 220–230°$, (h) $L_s = 230–240°$, (i) $L_s = 240–250°$, (j) $L_s = 250–260°$, (k) $L_s = 260–270°$, and (l) $L_s = 270–280°$.

thermal contrasts and slope flows (Cantor, 2007; Strausberg et al., 2005). Then, a rapid expansion to the east was initiated at Ls = 185° (Smith et al., 2002; Strausberg et al., 2005). No expansion to the west was observed (Strausberg et al., 2005). When dust approached the western flanks of Tharsis, new lifting centers arose in southeastern Tharsis (Daedalia and Solis Planitia) (Strausberg et al., 2005). The longest-lived lifting center (86 sols) was found in Syria Planum-Claritas Fossae (Cantor, 2007). By Ls = 193°, dust encircled the entire planet with lifting centers dominated in Syria Planum/Solis Planum/Daedalia Planum (Smith et al., 2002; Strausberg et al., 2005). Lifting centers over Hellas Planitia slowly diminished at this same time. The expansion phase (core of dust storm) came to an end at around Ls = 200° after which the fastest clearing was observed at high southerly latitudes with the slowest clearing in the northern hemisphere (Smith et al., 2002). High dust opacities were still found at around Ls = 210° in 0–20°N (Smith et al., 2002). For this storm, the decay phase was characterized by a latitudinal gradient in the rate of decrease in dust optical depth (Smith et al., 2002). This means that the decay phase appears at different seasons and latitudes (Strausberg et al., 2005). For example, the decay phase can start at southern latitudes earlier than at northern latitudes. The decay phase began at Ls = 200° and had a duration of about 97 sols (Ls = 263°) although clearing continued beyond that date. However, some dust lifting centers were still active as late as Ls = 214° (Strausberg et al., 2005). The atmospheric clearing continued until Ls = 304° when nominal seasonal levels of dust opacity were reached (Cantor, 2007). The decay phase duration defined by Cantor (2007) is different than the duration required for clearing back to the climatological averages.

The next planet-encircling event occurred in MY 28 (Figure 1b). In contrast to the global storm of MY 25, this event began at a much later seasonal date near Ls = 265°, after perihelion. However, we observed significant dust activity over the southern hemisphere before the onset of this global storm. Some possible precursor dust storms were observed over Hellas and the southern polar cap edge at Ls = 200–235° (Wolkenberg et al., 2018), which are illustrated by Figure 1b. The onset of this storm starts at Ls = 265° over regions from the South Pole
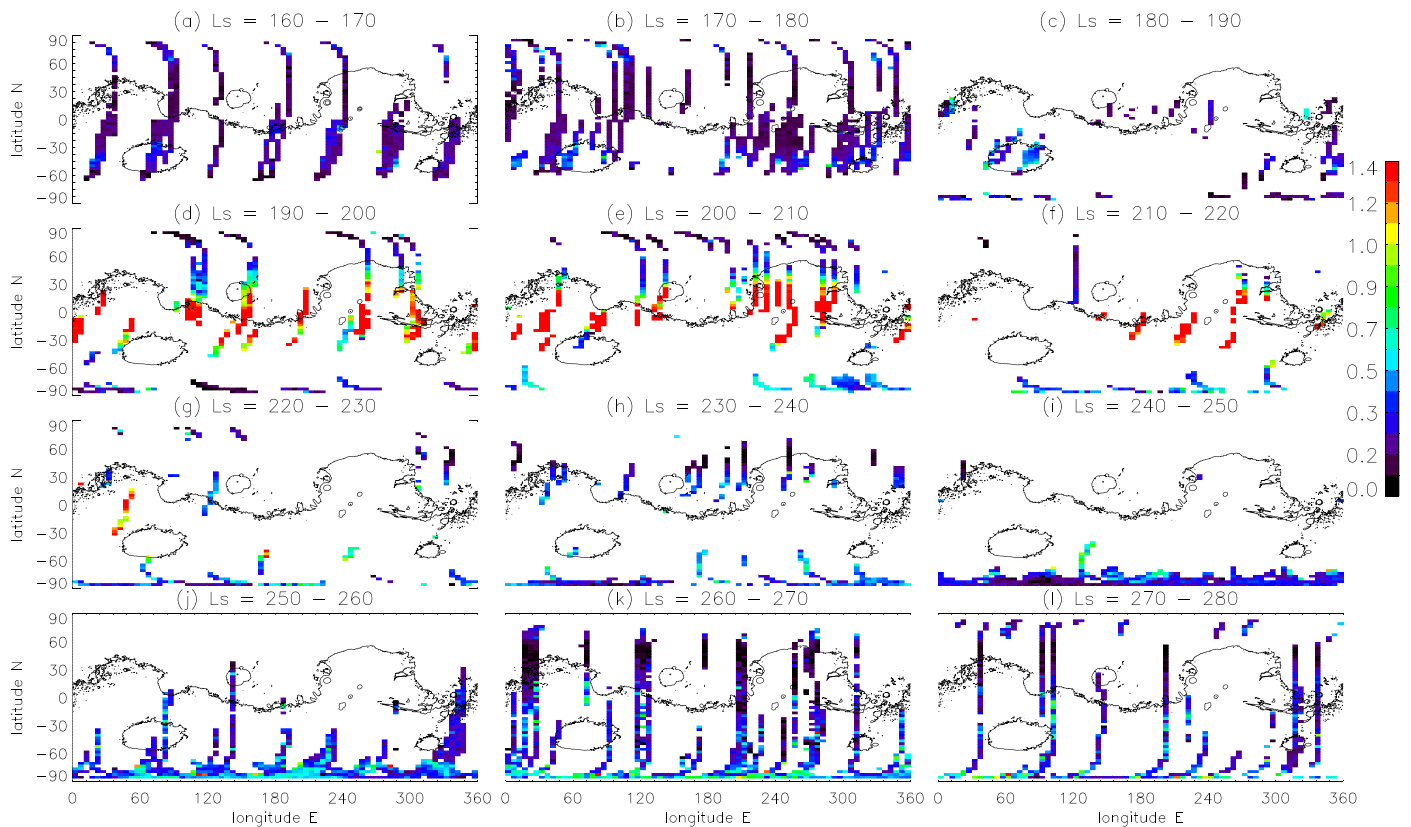
**Figure 3.** Spatial dust distributions (PFS) from Ls = 160° to 280° in MY 34 from 8 to 18 LT, (a) $L_s$ = 160–170°, (b) $L_s$ = 170–180°, (c) $L_s$ = 180–190°, (d) $L_s$ = 190–200°, (e) $L_s$ = 200–210°, (f) $L_s$ = 210–220°, (g) $L_s$ = 220–230°, (h) $L_s$ = 230–240°, (i) $L_s$ = 240–250°, (j) $L_s$ = 250–260°, (k) $L_s$ = 260–270°, and (l) $L_s$ = 270–280°.

to 40°N. A series of storms contributed to forming the global dust event in MY 28 (Smith, 2009). The dust storm in MY 25 had dust opacity larger than 1 as far south as 60°S, while the region where dust opacity exceeded unity for the dust storms of MYs 28 and 34 was more constrained to midlatitudes. During MY 28, dust opacity exceeded 1 over a latitudinal belt between 40°S and 40°N until around $L_s$ = 305°. Then the decay phase began, with opacity still larger than 0.5 until $L_s$ = 310° (Smith, 2009). The most recent GDS began in MY 34 at $L_s$ ~ 190° (Figure 1c). The core of this GDS extended from 50°N to around 40°S. Dust opacity gradually increased toward the South Pole with season. After $L_s$ = 210°, dust activity was pronounced southward of 40°S, and it gradually diminished at those latitudes until $L_s$ = 300° (Figure 1c). This phase was characterized by opacity ~0.5. Large dust opacity was still observed over south polar regions (>60°S) at $L_s$ = 260°, while dust was less visible over midlatitude regions at that time. Figures 1d–1f present the zonal means of atmospheric temperatures at 0.5 mbar (~25-km altitude) as a function of season and latitude. We observe increases of atmospheric temperatures at 0.5 mbar during the periods of high dust activity in all three years. The atmospheric response to dust is largest at around 0.5 mbar and at higher altitudes (Wilson & Richardson, 2000; Wolkenberg et al., 2018; Zurek et al., 1992). The temperature increase at 0.5 mbar during a GDS in the equatorial region and midlatitudes is the highest in MY 25. The GDS in MY 28 began just after perihelion when the solar heating is greatest. Meanwhile, the dust storm of MY 34 began during northern autumn, which is significantly earlier than perihelion. Comparing atmospheric temperatures at this level during the GDS against temperatures for years without global dust events, we observe an increase of around 20–30 K. While the atmospheric temperature increases observed in the southern hemisphere are primarily caused by direct solar heating of the dust, the corresponding increases observed in the northern hemisphere for all three years are instead due to the adiabatic compression of air from the descending branch of the intensified Hadley circulation caused by the response to the dust storm (Kass et al., 2016). In MY 34, we observed a second atmospheric temperature increase at a later season after the GDS over southern polar regions at around perihelion, but it was much weaker than the one during the GDS.

### 5.2. Spatial Analysis of GDSs

We present the spatial distribution of dust from $L_s = 160°$ to $280°$ in MY 25 obtained from TES measurements (Figure 2) to compare with MY 34 and MY 28 GDSs. Some local dust storms occurred over the northwest rim of Hellas at the beginning of the considered interval. By $L_s = 190°$, dust started expanding toward northeast reaching equatorial regions and west side of Tharsis. An abrupt explosion of dust was observed over Valles Marineris, equatorial regions, and Hellas in the next interval. Then, dust expanded to larger areas with the exception of Tharsis. Less dust activity was observed over Tharsis due to its high elevations. By $L_s = 220$, dust progressively began to diminish in the atmosphere, but it was mostly observed in the northern hemisphere. Dust was mostly constrained to lowlands in the northern hemisphere and appeared in regions featuring large topographic differences along the dichotomy boundary. Dust from regions around Valles Marineris moved westward to the southern part of Tharsis in the next $L_s$ interval. Dust opacity over Hellas was always larger than over other regions for the entire period considered. Eventually by $L_s = 280°$, dust opacities were less than 0.4 over the northern regions with Hellas opacities around 0.5–0.6.

We also studied the spatial distribution of dust aerosol after $L_s = 160°$ in MY 34 to investigate possible precursor storms. Figure 3 presents the evolution of the spatial distribution of atmospheric dust from $L_s = 160°$ to $280°$. Data are binned by $10°$ in $L_s$, by $5°$ in longitude, and by $3°$ in latitude. Similar to what was observed during MY 25, some signs of the onset of MY 34 storm were observed by PFS just after the northern autumn equinox at around $L_s = 190°$ (Figures 1c and 3c).

The ExoMars Trace Gas Orbiter (EMTGO) observed the onset of this GDS at $L_s \sim 188°$ (Vandaele et al., 2019). The Atmospheric Chemistry Suite instrument onboard the EMTGO spacecraft observed a local dust storm over Chryse Planitia in the $L_s$ range $184°$ to $187°$ (Ignatiev et al., 2019). According to results of assimilated Mars Climate Sounder data (Montabone et al., 2020, supporting information), the MY 34 storm began its activity over Chryse Planitia and Arabia Terra (Meridiani Planum). Figure 3a showed an increase of dust opacity up to ~0.4 over Aonia Terra (50°S, 280°E), the northern rim of Hellas and Noachis Terra (50°S, 10°E). Relatively large dust loads were also observed by Atmospheric Chemistry Suite-EMTGO below 15 km at $L_s = 168.75°$ in the latitude range, 39–43°S which corresponds to latitudes of the Hellas region (Vandaele et al., 2019). Dust activity was then observed westward of Argyre (Aonia Terra) with opacity ~0.5 (Figure 3b). Acidalia (30–60°N, 300–360°E) and Utopia (30–60°N, 80–140°E) Planitia are regions where local dust storms were imaged at $L_s = 181°$ by Mars Color Imager (MARCI) (Malin et al., 2018a, 2018b, 2018c). The PFS instrument was not able to observe these local dust storms seen by MARCI well because of sparse data coverage during this period ($L_s = 180–190°$; Figure 3c). However, in the $L_s$ interval from $L_s = 160°$ to $180°$ (Figures 3a and 3b), dust activity was indeed observed by PFS where local dust storms have been observed by MARCI. There are spots where PFS dust opacities are higher than the background along the few PFS ground-tracks passing across the Utopia Planitia and Acidalia Planitia. In addition, in the $L_s$ interval (170–180°; Figure 3b), the atmosphere over Hellas was dustier compared to the previous $L_s$ interval with pronounced local dust activity over the northwestern rim and the southeastern region of Hellas. Dust was also distributed westward of Argyre over a wide region extending from 280°E to 200°E at around 50°S (Sirrenium Terra). Thus, we observe as many as four regions where precursor dust storms could have originated before $L_s = 181°$.

These regions are Acidalia and Utopia Planitia imaged by MARCI, Hellas basin, and Aonia-Sirrenium Terra. These areas might be locations of independently developed precursor dust storms in MY 34. In spite of sparse PFS data, in the following $L_s$ interval (Figure 3c), we note that the dust optical depth increased to around 0.7 in Xanthe Terra (southern region of Chryse Planitia, 330°E, 10°N) and Arabia Terra (20°E, 20°N). These regions are located near the meridional corridors (Chryse Planitia) where dust is often transported from the north to the south (Wang & Richardson, 2015). We also observed larger opacity in the eastern half of the Hellas basin compared to the western half. According to images from MARCI (Malin et al., 2018c, 2018d), substantial dust lifting also originated in the southern hemisphere by around $L_s = 188°$ along the receding southern polar cap. MARCI observed that storms started in the southern hemisphere, merging with those that originated along and north of equator (Malin et al., 2018c, 2018d). By around $L_s = 193°$, dust became distributed globally (Guzewich et al., 2019; Malin et al., 2018d, 2018e). PFS also observed a rapid increase of dust opacity (up to 3 or more) from $L_s = 190–200°$ between 45°S and 45°N (Figure 3d). Dust
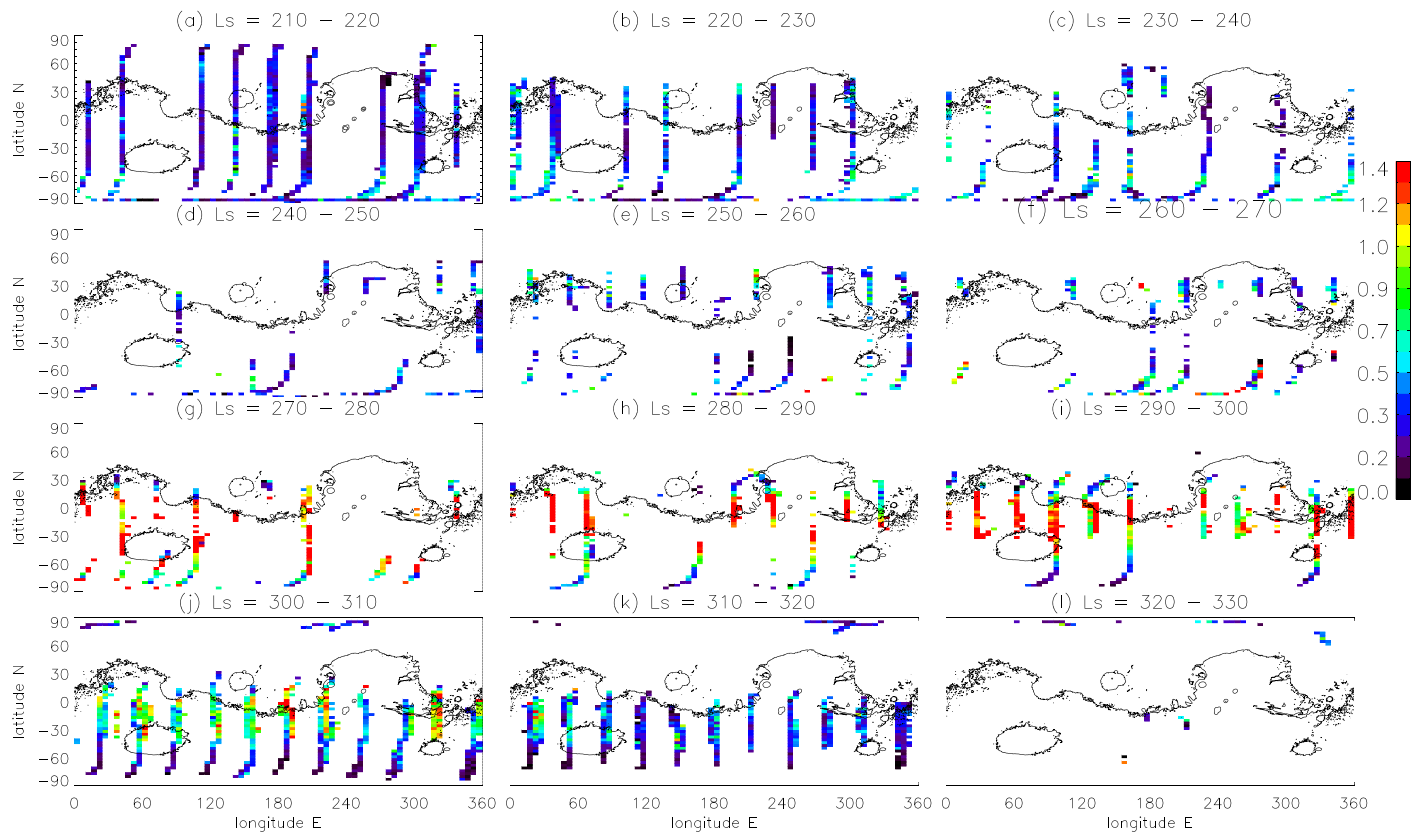
**Figure 4.** Spatial dust distributions (PFS) from Ls = 210° to 330° in MY 28 from 8 to 18 LT, (a) $L_s$ = 210–220°, (b) $L_s$ = 220–230°, (c) $L_s$ = 230–240°, (d) $L_s$ = 240–250°, (e) $L_s$ = 250–260°, (f) $L_s$ = 260–270°, (g) $L_s$ = 270–280°, (h) $L_s$ = 280–290°, (i) $L_s$ = 290–3000°, (j) $L_s$ = 300–310°, (k) $L_s$ = 310–320°, and (l) $L_s$ = 320–330°.

opacities continued to increase during the next $L_s$ interval (Figure 3e), while MARCI started observing a decay phase at around $L_s$ = 205° (Malin et al., 2018f, 2018g). We are unable to distinguish the starting point of the decay phase for the GDS in MY 34 from the PFS observations in Figure 3. However, despite the poor spatial coverage, PFS observed significant opacities (around 1.5) at Tharsis and northwest of Hellas from $L_s$ = 210–230° (Figures 3f and 3g). The atmospheric dust then progressively decreased by settling down on the surface (Figure 3h). It is worth noting that dust activity also occurred close the southern polar regions during the period from $L_s$ = 200° until $L_s$ = 280° (Figures 3j–3l).

Figure 4 presents the spatial distribution of dust for the $L_s$ interval from 210° to 330° in MY 28. As was seen in Figure 1b, we observed a significant increase in dust opacity up to 0.6 over southern polar regions but also over Elysium Planitia in the northern hemisphere before onset of the MY28 GDS at $L_s$ = 265°. The dust storm then developed into a global event from $L_s$ = 270° until 300°. Dust opacity around 0.9 was still observed after $L_s$ = 300° as gradually decreased with season. Comparison with the MY 34 GDS spatial distributions (Figure 3) shows that dust in the MY 28 storm during its decay phase was not distributed toward southern polar regions. Instead, we observed a quite clear atmosphere at $L_s$ = 300–320° over latitudes higher than 60°S in MY 28. A similar behavior of spatial dust distributions was also observed in the MY 25 storm during its decay phase. Another characteristic feature was that the atmosphere over the Tharsis region contained more dust in MYs 28 and 34 (Figures 4h, 4i, and 3d–3f) than in MY 25 (Figures 2d–2f) at maximum dust activity at $L_s$ = 280–300° and $L_s$ = 190–220°, respectively.

### 5.3. Time Series of Dust Opacities

Cores of storms were found and defined as locations with zonally averaged dust opacity larger than 1 in each bin. Zonally averaged dust opacity exceeding unity in MY 25 was observed for the region from 50°S to 20°N
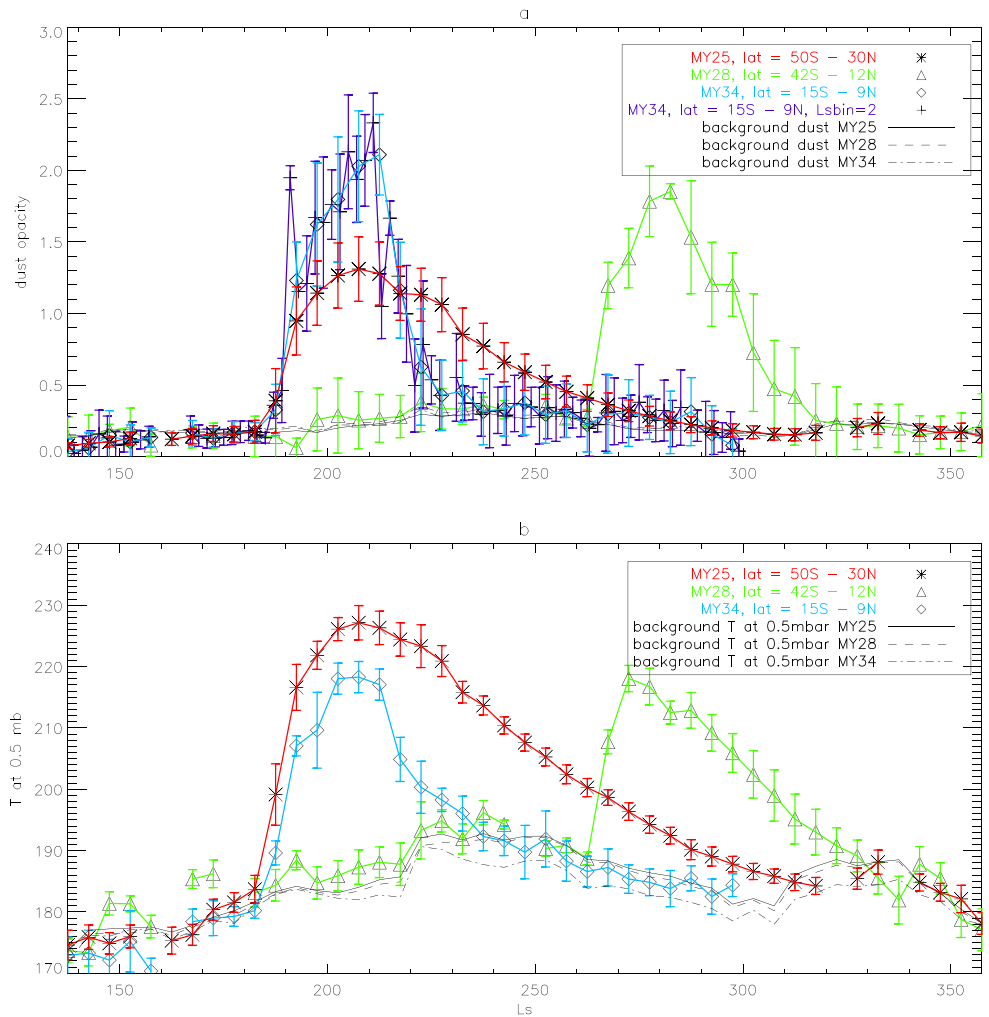
**Figure 5.** Seasonal variations of zonally averaged (a) dust opacities and (b) atmospheric temperatures at 0.5 mbar for MYs 25, 28, and 34 with standard deviations in each bin. Dust opacity was binned by 5° in Ls, by 3° in latitude, and by 5° in longitude, and then they were averaged zonally. The same treatment of data was used to calculate the background level of dust opacity (solid line for MY25, dashed line for MY 28, and dotted-dashed line for MY 34). The background level of dust opacity is different for three MYs because the different ranges of latitudes are taken into account.

for $L_s$ = 190–221°. Cores of storms in MY 28 and in MY 34 with dust opacity larger than 1.75 and 1.9 in each bin were constrained to nearly 42°S to 12°N and to 15°S to 9°N, respectively. We selected these values because they were within 1 standard deviation from the maxima of Gaussian functions fitted to each dust storm for $L_s$ range from 190° to 221° in MYs 34 and 28 and from 270° to 297°. Peaks of dust opacity in MY 25 and MY 34 were observed at similar $L_s$ (Figure 5a). The MY 34 maximum was shifted in season due to the latitudinal range taken into account to plot the variation of dust distribution with season. Dust opacity peaked at the same $L_s$ like in MY 25 when the range of latitudes for the core was extended to 12°N. The MY 25 and MY 34 storms started at similar times. We observe an increase in atmospheric dust opacity suddenly in all MYs due to dust lifting (Figure 5a). The curve of the seasonal variation of dust opacity is asymmetric with respect to maximum of dust opacity in MY 25 (Figure 5a), with much faster growth than decay. On the contrary, a longer expansion with respect to decay phase was observed in MY 34. The opacity changed rapidly from 0.25 before the storm to values larger than 1 in just a couple of days in MY 25. Dust opacity larger than 1 was observed from $L_s$ = 190° until 228° in MY 25 (Figure 5a). This is the longest seasonal interval when dust opacity exceeds 1 among the other GDSs considered here (MY 28 and MY 34). The
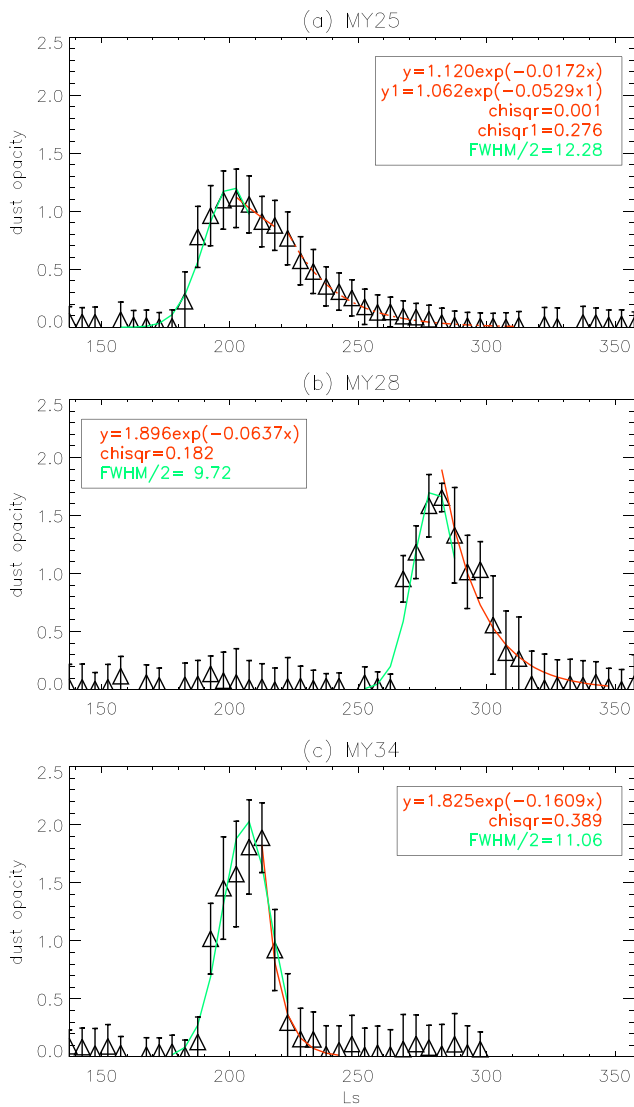
**Figure 6.** Time series of dust opacities (triangle symbols) with standard deviations in MY 25 (a), MY 28 (b), and MY 34 (c). Fit of Gaussian (green line) and exponential decay function (red line) to dust opacities without background dust opacities are plotted. The decay phase in MY 25 is fitted by two exponential decay functions (red solid and dashed line). "y" and "y1" mean the model values of Gaussian functions in MY 25, MY 28, and MY 34. The numerical value in the exponential function gives the decay constant. "Chisqr1" and "chisqr" are the chi-squared quality factors of the fit for exponential decay functions in all MYs.

seasonal dust distribution in MY 34 was also plotted with 2° bin in $L_s$ (blue line) to show dust variation in more details. A separate and large peak was observed at $L_s$ around 190° which was not evident when the seasonal binning was 5°. A detailed analysis of observations available in this $L_s$ range revealed that large dust opacities around unity were measured over regions of Arabia Terra (5–20°N, 25–27°E) near the Cassini crater.

The background level of dust activity was calculated for each bin in $L_s$ and latitude taking into account all PFS MYs without GDSs. We selected data of dust opacities from PFS MYs including MY 27 and MYs 29–33. Then we calculated the values of dust opacity for each bin with latitude, $L_s$, and longitude (3° × 5° × 5°), respectively. Then we zonally averaged them. We plotted the background level of dust opacities independently for each storm because we selected different core regions for each storm. Along with the observed increases in dust opacity, atmospheric temperatures at 0.5 mbar were observed to grow immediately after the onset of the three global storms (Figure 5b). The timing of the MY 25 maximum temperature value was closely aligned with the timing of the maximum dust opacity. For the other dust storms, the atmospheric temperatures peaks occurred somewhat earlier in season than dust opacity maxima. We defined the climatological values of atmospheric temperatures at 0.5 mbar as a mean of atmospheric temperatures for all MYs from PFS data excluding MY 28 and MY 34. They are plotted in Figure 5b. The procedure of calculation is the same as it was for background dust level.

It is worth noting that the maximum of dust opacity in MY 34 exceeded 2.1 when the retrievals are binned and is largest among the three storms (Figure 5a). A similar behavior of dust storm (large value at peak) in MY 34 was also observed over the Curiosity landing site (Guzewich et al., 2019). We also observed some possible precursor dust storms as a component of "background dust activity" in MY 28 beginning at $L_s = 200°$, which is better illustrated in Figure 1b. The core of MY 28 storm starts at $L_s = 270°$. If we assume that these possible precursor dust storms could be interpreted as representing the background level of dust activity from $L_s = 200°$ to 270° in MY 28, then the MY 28 storm can be similar to the others. Indeed, the increases of dust activity were found from $L_s = 200°$ to 270° and $L_s = 310°$ to 340° (Figure 5a). Figure 5a shows that possible precursor dust storms were component of background level of dust opacities in MY 28.

Figure 6 presents the seasonal distribution of zonally averaged dust opacity after subtraction of background level of dust activity. This way, the clear behavior of storms was presented. To better characterize or find similarities and differences between storms, exponential decay and Gauss functions were fitted to seasonal zonally averaged dust opacities to define the decay and expansion phases, respectively (Figure 6). The duration of expansion phase could be described by the half of full width at half maximum derived from the fit of Gaussian function to the dust opacities.

It turned out that expansion phases of three storms were very similar. They differed only 1° of $L_s$ between each other. The MY 34 storm had a medium expansion phase around 11° of $L_s$ (19 sols) compared to MY 28 with 10° of $L_s$ (15 sols). The longest expansion time with 12° of $L_s$ was in MY 25 (21 sols). In contrast to expansion phases, each GDS had a unique value of decay phase. The coefficient in the exponential expression is the decay constant (multiplicative factor at x ($L_s$); Figure 6). There was no particularly long decay phase of dust opacity in the MY 34 storm as it occurred in MY 25 and MY 28 storms. Similarities in the decay phases were found in MY 25 and MY 28. However, we divided the decay phase into two seasonal intervals in
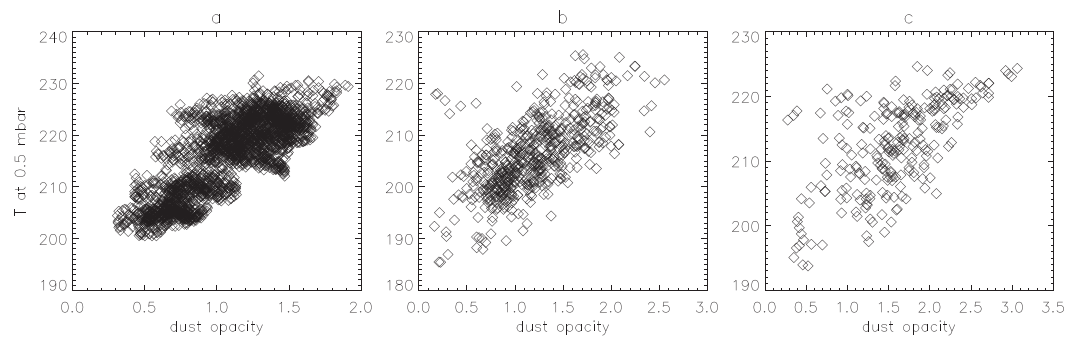
**Figure 7.** Scatter plots of dust opacities as a function of atmospheric temperatures at 0.5 mbar for (a) MY 25, (b) MY 28, and (c) MY 34.

MY 25 to describe it better. The decay constants were 0.0529 ± 0.0183 (1/19° of $L_s$) in MY 25 for the second part of decay phase and 0.0637 ± 0.0072 in MY 28. The first part of the decay phase in MY 25 lasted 10° of $L_s$ (16 sols) with the decay constant equaling 0.0172. The lifetime of the storm (58° of $L_s$ or 94 sols) was longer when we also consider the duration of the first part of the decay phase. We compared the decay constants for the second part of the decay phase in MY 25 with that in MY 28. After 20° (32 sols) and 17° (29 sols) of $L_s$, respectively, the population of dust opacity decreased exponentially (by 1/e). On the other hand, the storm in MY 34 had the shortest decay phase. The decay constant was estimated to be 0.16, and the mean lifetime was around 6° of $L_s$ (10 sols). This means that after around 24° of $L_s$ (38 sols), the dust opacity reached the background level. The settling down to the surface was two and half times faster in MY 34 than in the other storms. This result is unexpected because the two dust storms in MYs 25 and 34 started in the same season should have similar development and decay phases taking into account the similar atmospheric conditions. We also evaluated a skewness of these three GDS series, which gave results similar to the Gaussian function fits. We obtained for GDSs in MY 25: +0.91, MY 28: +1.36, and MY 34: +1.76. These positive values mean that each GDS time series is asymmetric with respect to their maxima with each series having a long decay tail. A larger positive value for the skewness indicates a faster decline in dust opacity. The largest value of the skewness is for the GDS of MY 34. This is in agreement with the decay constant obtained from the fit of the exponential decay function, which also indicated that the fastest decay phase was for the MY 34 GDS.

Only the time of expansion phase is similar. If the dust aerosols were similar sizes for the three storms, they should settle out of the atmosphere at about the same rate for all the storms unless strong vertical winds, cloud formation, or something else occurs. Thus, the reason of fast settling down could be other mechanisms associated with the atmospheric circulation. One-dimensional (vertical) simulations of aerosol transport showed that atmospheric motions were key factors in storm decays (Murphy et al., 1990). Moreover, an assumption of disk-like particles showed a good agreement between measured dust optical depths over Viking 1 lander locations and one-dimensional models. However, this model was not able to maintain the initial size distribution for particles in the 1- to 10-μm range, which were predicted by Mariner IRIS results of dust storm in 1971. Thus, a two-dimensional model was developed in which spherical particles were more consistent with measured dust optical depth rate over Viking 1 lander location. Moreover, the assumption of spherical particles implied a latitudinal variation of seasonal dust opacity decreases (decay constant) and evolution of particle size distribution. The evolution of particle size distribution and dust opacity declines (decay constants) were much more slowly in the ascending branch of Hadley circulation than in the descending branch (Murphy et al., 1990). The aerosol models showed that the atmospheric circulation played a key role during the decay phases of dust storms in controlling the settling down rate of dust grains of different sizes.

Previous works on decay constants provided similar values for some regions (Cantor, 2007; Fenton et al., 1997). Fenton et al. (1997) found 42 sols as a decay constant for regions at 55–65°S in dust storm 1971 (MY 9) observed by the Mariner orbiter. The decay constant over Claritas Fossae region during the MY 25
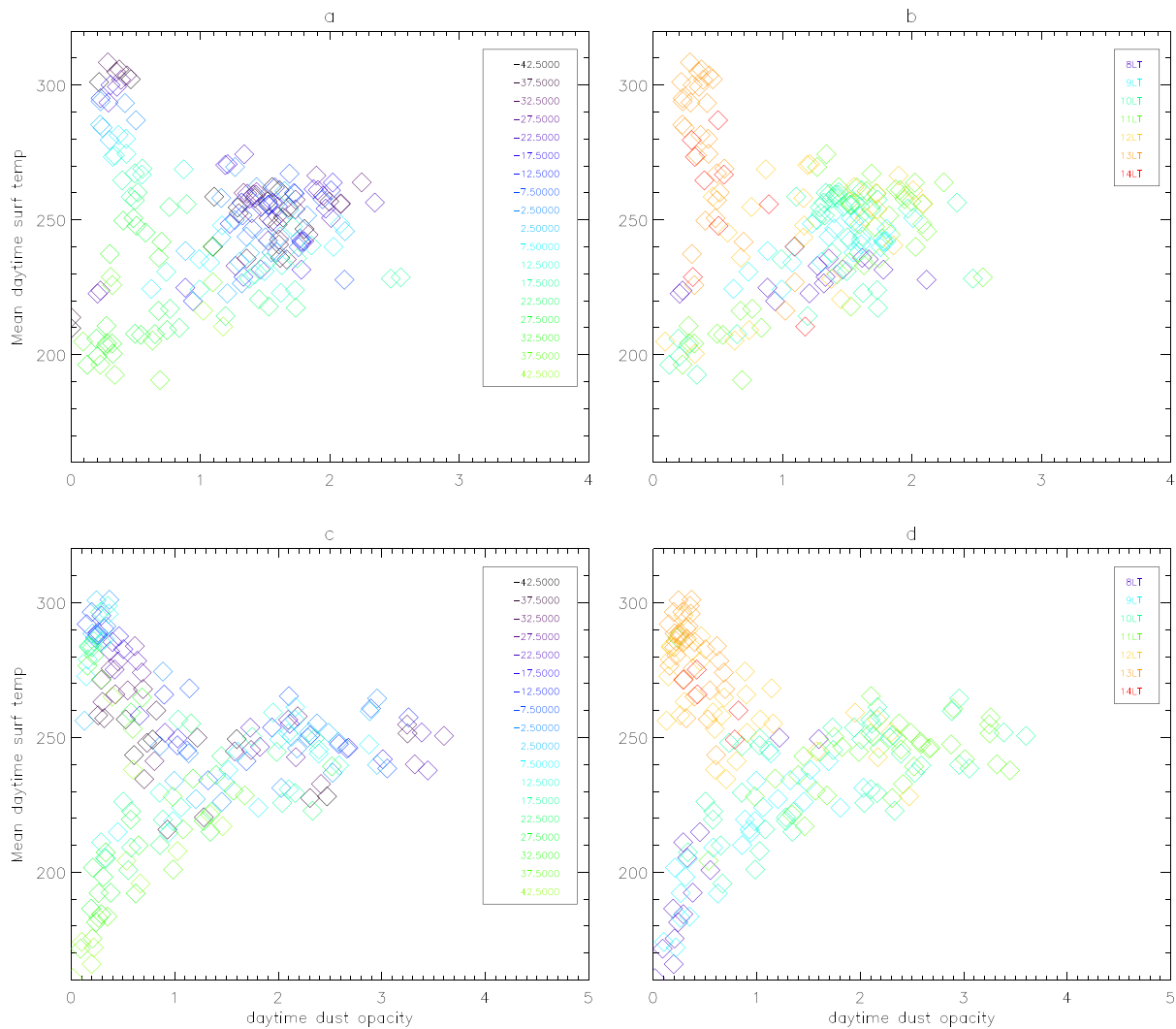
**Figure 8.** Scatter plots with daytime dust opacities as a function of mean daytime surface temperatures for MY 28 (a,b) and for MY 34 (c,d) in $L_s$ intervals from 250° to 330° and 170° to 240°, respectively. Colors in (a) and (c) represent latitudes from 42.5°S to 42.5°N. Colors in (b) and (d) represent local time. Data are available for LTs from 8 to 14.

storm was smaller, around 30 sols (Cantor, 2007). However, Cantor (2007) divided the decay phase into two time intervals. He found smaller decay constants during the second interval of the decay phase for other regions. Likely, the small decay constant during the second interval of the decay phase was estimated for the "background" dust occurring every year. Cantor (2007) derived decay constants corresponding to both the global storm and "background" dust activity. During the second part of the decay phase, the main dust activity due to the global storm decreased the level of background activity and thus the decay constants became smaller. The background dust occurring every year contains the typical behavior of dust activity during the dust season ($L_s$ = 135–360°) including regional and local dust storms. Our results showed larger decay constants (shorter mean lifetimes) compared to those presented by Fenton et al. (1997) for the equatorial region. Likely, this was due to the fact that the "background" dust activity was subtracted from our data. Then the exponential function was fitted to the data (Figure 6).

### 5.4. Impact of GDS on Atmospheric and Surface Temperatures

Dust can be investigated indirectly by using atmospheric temperatures at 0.5 mbar. We plot dust opacity as a function of atmospheric temperatures at 0.5 mbar for three GDSs (Figure 7). As expected, a strong correlation of dust with atmospheric temperatures at 0.5 mbar is observed. Atmospheric temperatures at this level
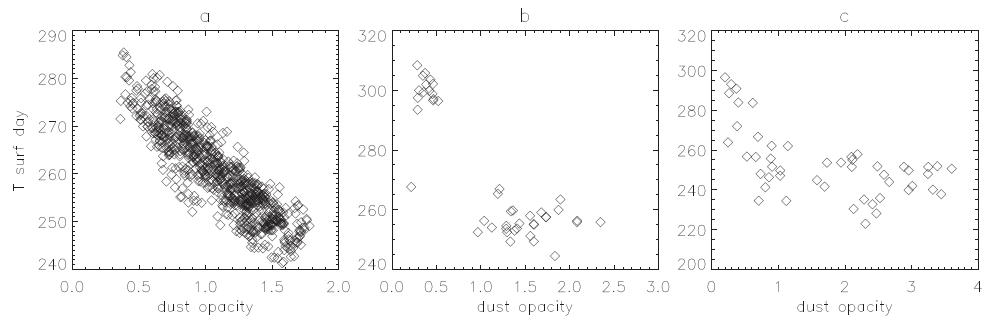
**Figure 9.** Scatter plots of dust opacity as a function of daytime surface temperatures for global dust storm seasons in MY 25 (a), MY 28 (b), and MY 34 (c). (a) Data are binned in latitude, longitude, and $L_s$ ($5° \times 7.5° \times 10°$), respectively, for the $L_s$ range from 180° to 240° and the latitude range from 10°S to the equator. (b) Data are averaged zonally and binned in latitude and Ls ($5° \times 10°$) in the season from $L_s = 240°$ to 350° and the latitude range from 45°S to 15°S. (c) Data are averaged zonally and binned in latitude and $L_s$ ($5° \times 10°$) in the season from $L_s = 180°$ to 260° and the latitude range from 45°S to 5°N.

increase with dust opacity for each MY. Figure 7a presents the relationship between dust and atmospheric temperatures at 0.5 mbar in MY 25 during GDS. Each point represents data binned in latitude, longitude, and Ls ($3° \times 5° \times 10°$), respectively. We selected daytime data only in the latitudinal range around the equator (12°N to 12°S) and from the Ls = 180–240° range when dust opacity is relatively large. The TES spectrometer performs measurements at two observation LTs, at about 2:00 and 14:00 LT. The atmospheric temperature range is from 200 to 230 K for dust opacity variations from 0.3 to 2 in MY 25. The heating rate of the atmosphere can be a characteristic feature of this dust storm depending on the chemical composition and the size distribution of the dust aerosol. For MY 28, data are taken from the Ls = 260–330° interval, and the LT range is from 9:00 to 18:00 to be comparable with the data from MY 25 (Figure 7b). Atmospheric temperatures at 0.5 mbar increase along with dust opacities over southern latitudes from the equator to 42°S. This region is more exposed to the Sun than northern latitudes during the season of the GDS (after perihelion). The maximum atmospheric temperatures at 0.5 mbar are around 220–225 K and correspond to dust opacities around 2.5. In MY 34, again, a clear trend of atmospheric temperatures at 0.5 mbar with dust is observed (Figure 7c). The data are selected from the Ls = 180–240° range and around the equator (12°S to 12°N). The atmospheric temperatures increase from 195 to 225 K with dust opacities from 0.3 to 3.2, respectively.

We also investigate the relationship between mean daytime surface temperatures and daytime dust opacities for midlatitude regions in MY 28 and MY 34 (Figures 8). Each point corresponds to data zonally averaged, binned in latitude, $L_s$, and LT ($5° \times 10° \times 1$ hr). The local time range is from 8 to 14 LT. For both years, we observe a special behavior of dust opacities with surface temperatures during the day. Temperature around 250 K is found at maximum dust opacities in both years. It decreases with dust opacity increases when the temperature is higher than 250 K, while it increases with dust opacities for temperature less than 250 K. We plot latitude bins and corresponding LT bins in different colors to analyze the spatial distribution of dust opacities with surface temperatures (Figure 8). In MY 28, mean daytime surface temperatures higher than 250 K are mostly measured in the southern hemisphere and over the equator. In this region we have observations mainly at two LTs: 10–11 LT and after 13 LT (Figure 8b). Before noon, the dust opacities are very large with surface temperatures around 250 K, while after 12 LT, surface temperatures increase with decreasing dust opacity (<0.5) in the atmosphere. Lower surface temperatures than 250 K are found in the northern midlatitude region. Observations there are performed at morning times from 8 to 11 LT. The lower surface temperatures there are expected according to season and latitude. Surface temperatures over northern latitudes increase with dust opacities approaching to around 250 K. A similar trend of daytime dust opacities as a function of mean daytime surface temperatures is also observed in MY 34 (Figures 8c and 8d). Southern midlatitudes and the region over the equator are characterized by a decrease of surface temperatures with increasing dust opacity. Observations over these regions mostly take place from 11 to 14 LT. The surface temperature increases along with dust opacity over the northern hemisphere in the morning at 8–10 LT. As it was for MY 28, the maximum of dust opacity is observed at around 250 K.
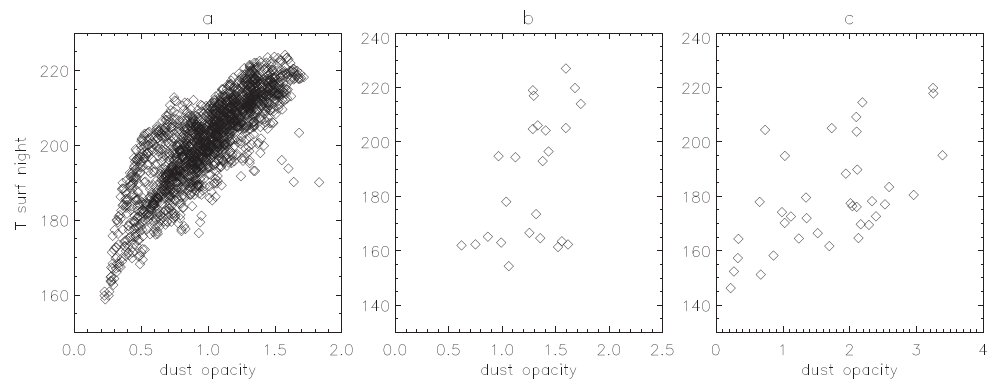
**Figure 10.** Scatter plots of daytime dust opacity against nighttime surface temperature. (a) Data are binned in latitude, longitude, and $L_s$ ($5° \times 7.5° \times 10°$), respectively, for the $L_s$ range from 190° to 250° and the latitude range from 5°N to 40°N in MY 25. (b) Data are averaged zonally and binned in latitude and $L_s$ ($5° \times 10°$) in the season from $L_s = 240°$ to 350° and the latitude range from 45°S to 10°N for 18–9 LT in MY 28. (c) Data are averaged zonally and binned in latitude and $L_s$ ($5° \times 10°$) in the season from $L_s = 180°$ to 260° and the latitude range from 45°S to 45°N for 18–9LT in MY 34.

For both years, we also note that surface temperatures are relatively constant whenever dust opacity is greater than about 1–2.

Comparing the two GDSs that occurred during MY 28 and MY 34 (Figure 8), we observe a similar distribution of surface temperatures with respect to LT. Southern and equatorial latitudes were mostly observed during the afternoon, while northern latitudes were observed during the morning. However, the two GDSs began at different seasons. Therefore, the sun illumination conditions were different. For example, it is clear that in MY 28, surface temperatures are warmer at 8 LT than at 10 LT because they are measured for regions further southward from the equator. Southern regions are more illuminated than northern regions near perihelion; thus, surface temperatures and dust opacities are larger at 8 LT (42–35°S) than at 10 LT (35–42°N). This trend between surface temperatures and dust opacity (Figure 8) helps explain the radiation budget in the Martian atmosphere in the presence of high dust loads. During the day, the dust is heated by the solar radiation, and contemporaneously this layer of dust prevents the heating of the lower atmosphere and surface below. This leads to the decrease of surface temperature and the cooling of the atmosphere close to the surface dependent on dust loads (Wolkenberg et al., 2018). For example, in Figures 8a and 8b in MY 28, we observe almost the same region around 7.5–12.5°N at around 11–12 LT for different dust opacities from 0.5 to 2. For these values, we observe different surface temperatures from 280 to 250 K. Surface temperatures decreased to 250 K at 11–12 LT for dust opacities around 2. Simultaneously, we observe at the same LT and region surface temperatures around 280 K but for opacity around 0.5. For dust opacities larger than 1–2 at noon, surface temperatures are constant. For locations with a relatively small amount of dust less than 0.3, surface temperatures are around 300–310 K during the afternoon. When dust increases, surface temperatures decrease to around 250 K before noon. Afternoon surface temperature increases when dust decreases over the same region (southern latitudes). Atmospheric dust prevents the solar radiation from penetrating to the layers close to the surface, and as a result, surface temperature decreases by the reduction of solar heating. The decrease of daytime surface temperatures with dust opacity is also observed in MY 25 from the TES data (Figure 9a). We note a similar behavior in MY 28 (Figure 9b) and MY 34 (Figure 9c). In MY 28, there are a lot of gaps, particularly between 0.5 and 1 of dust opacity (Figure 9b). However, the drop of daytime surface temperatures is clearly observed until 1.5 of dust opacity (Figure 9b).

For dust opacities larger than 1.5, a characteristic plateau is observed in MY 28 and MY 34 where daytime surface temperatures no longer decrease with increasing dust opacity (Figure 9c). However, this could be due to observations being at different LTs. In MY 25, this plateau is not evident because measurements were performed at a LT near 14:00.

We also investigate the relation between daytime dust opacities and nighttime surface temperatures (Figure 10). In each Martian year considered in Figure 10, we observe an increase in nighttime surface temperature with dust opacity. However, the rate of these increases appears to be different in each Martian year.

In these nighttime observations, the atmosphere (and dust) are warmer than the surface. The more dust there is in the atmosphere, the more warm downward radiation from the dust is received at the surface increasing the surface temperature. In the clear atmosphere, the surface cools off during the night through the emission of thermal infrared radiation with little compensating downward radiation from the atmosphere.

## 6. Summary and Conclusions

We report on seasonal and spatial variations of dust opacities in MY 34 obtained from measurements performed by PFS onboard Mars Express spacecraft. Additionally, we also present the evolution of dust opacities in MY 25 obtained from TES measurements and in MY 28 from PFS observations to find similarities and differences between the GDSs that occurred in those three years. The two GDSs during MY 25 and MY 34 were equinoctial events encircling the whole planet at about $L_s = 193$. Similarities are also found in the onset of MYs 25 and 34 storms such as a local dust storm over the northern rim of Hellas (dust opacity >0.4) that was observed in both MY 25 and MY 34. In MY 25, dust storm area expanded east over the next several days. In MY 34, we also observed dust over on the eastern side of Hellas basin. Some similar dust occurrences in Arabia Terra and Utopia Planitia were also found before the expansion phase in MY 25 and MY 34. A peak of dust activity at $L_s = 190°$ in the expansion phase was observed in Arabia Terra near Cassini crater in MY 34. However, there were differences as well. For example, PFS observed dust over regions further to the north than TES did in MY 25. The MY 28 dust storm began after perihelion near the southern summer solstice contrary to the dust events in MYs 25 and 34, which occurred much earlier during the season. Hence, the specific features of the MY 28 storm were different than the others. We observed some possible precursor dust storms mainly over the Hellas region and the southern polar cap edge long before the onset. These features were not observed before the equinoctial dust storms on this scale. However, these possible precursor dust storms in MY 28 were a component of background dust activity. After subtraction of background dust opacities, the separate analysis of each GDS was possible. These studies revealed that the time of expansion phase of each GDS was similar. They differed between each other by 1° of $L_s$. However, the data binning by 2° in $L_s$ showed a separate peak of dust opacity near unity in the expansion phase of MY 34 GDS, which could imply a different expansion phase. In contrast to the expansion time, each GDS had a unique duration of the decay phase. However, the removal of background activity showed that the two GDSs in MY 28 and MY 25 had similar decay constants (0.06 and 0.05, respectively) although they started in different season at different atmospheric conditions. By contrast, GDS in MY 34 was characterized by two and half times faster decay constant than other both storms. This implied a shorter mean lifetime of this storm compared to storms in MY 25 and MY 28. The spatial distribution of the MY 28 storm was more limited to the regions over the southern hemisphere than the storm of MY 34. During the expansion phase of the global storms, dust in MY 25 and MY 34 was more distributed toward the north (50°N) than it was during in MY 28.

A clear relation between atmospheric temperatures at 0.5 mbar and dust opacities is presented. As has been found earlier, we confirm that atmospheric temperature increases at 0.5 mbar were mainly due to dust opacity increases. We also observed a large decrease in daytime surface temperatures with increasing dust opacity. However, in MY 34, daytime surface temperatures remained nearly constant reaching a characteristic plateau when dust opacity exceeded 2. A similar situation was observed in MY 28, but the trend was less obvious because the maximum dust opacity was ~2–2.5. In MY 28 and MY 34, we observed what appears to be a drop of dust opacities from 10–11 LT to 13–14 LT at southern low latitudes. Contemporaneously, we noted an increase of daytime surface temperatures at those LTs. It is not clear if this afternoon increase of surface temperatures was due to the decrease in dust with solar radiation better able to reach the surface. Finally, during all three global storms, we observed that nighttime surface temperatures increased with increasing dust opacity (measured during the day).

The physical mechanisms that govern the initiation, growth, and decay of GDSs on Mars are still not well understood. While there are broad similarities in the behavior of these global storms, each storm exhibits its own unique characteristics depending on many factors including the season in which it begins and the locations where dust raising is initiated. The new observations of the MY 34 global storm along with a comparison of previous global storms observed in MY 25 and MY 28 presented here provide the crucial observational input that models will be able to use to better understand the evolution of GDSs and the Mars dust cycle in general.

# References

Bandfield, J. L., & Smith, M. D. (2003). Multiple emission angle surface–atmosphere separations of Thermal Emission Spectrometer data. *Icarus*, *161*(1), 47–65. https://doi.org/10.1016/S0019-1035(02)00025-8

Cantor, B. A. (2007). MOC observations of the 2001 Mars planet-encircling dust storm. *Icarus*, *186*(1), 60–96. https://doi.org/10.1016/j.icarus.2006.08.019

Cantor, B. A., James, P. B., Caplinger, M., & Wolff, M. J. (2001). Martian dust storms: 1999 Mars Orbiter Camera observations. *Journal of Geophysical Research*, *106*(E10), 23,653–23,687. https://doi.org/10.1029/2000JE001310

Christensen, P. R., Bandfield, J. L., Hamilton, V. E., Ruff, S. W., Kieffer, H. H., Titus, T. N., et al. (2001). The Mars Global Surveyor Thermal Emission Spectrometer experiment: Investigation description and surface science results. *Journal of Geophysical Research*, *106*(E10), 23,823–23,871. https://doi.org/10.1029/2000JE001370

Conrath, B. J., Pearl, J. C., Smith, M. D., Maguire, W. C., Christensen, P. R., Dason, S., & Kaelberer, M. S. (2000). Mars Global Surveyor Thermal Emission Spectrometer (TES) observations: Atmospheric temperatures during aerobraking and science phasing. *Journal of Geophysical Research*, *105*(E4), 9509–9519. https://doi.org/10.1029/1999JE001095

Fenton, L. K., Perl, J. C., & Martin, T. Z. (1997). Mapping Mariner 9 Dust Opacities. *Icarus*, *130*(1), 115–124. https://doi.org/10.1006/icar.1997.5810

Formisano, V., Angrilli, F., Arnold, G., Atreya, S., Bianchini, G., Biondi, D., et al. (2005). The Planetary Fourier Spectrometer (PFS) onboard the European Mars Express mission. *Planetary and Space Science*, *53*(10), 963–974. https://doi.org/10.1016/j.pss.2004.12.006

Giuranna, M., Formisano, V., Biondi, D., Ekonomov, A., Fonti, S., Grassi, D., et al. (2005b). Calibration of the Planetary Fourier Spectrometer long wavelength channel. *Planetary and Space Science*, *53*(10), 993–1007. https://doi.org/10.1016/j.pss.2005.02.007

Giuranna, M., Formisano, V., Biondi, D., Ekonomov, A., Fonti, S., Grassi, D., et al. (2005a). Calibration of the Planetary Fourier Spectrometer short wavelength channel. *Planetary and Space Science*, *53*(10), 975–991. https://doi.org/10.1016/j.pss.2004.12.007

Giuranna, M., Wolkenberg, P., Grassi, D., Aronica, A., Aoki, S., Scaccabarozzi, D., et al. (2019). The current weather and climate of Mars: 12 years of atmospheric monitoring by the Planetary Fourier Spectrometer on Mars Express. *Icarus*. https://doi.org/10.1016/j.icarus.2019.113406

Grassi, D., Ignatiev, N. I., Zasova, L. V., Maturilli, A., Formisano, V., Bianchini, G. A., & Giuranna, M. (2005). Methods for the analysis of data from the Planetary Fourier Spectrometer on the Mars Express mission. *Planetary and Space Science*, *53*(10), 1017–1034. https://doi.org/10.1016/j.pss.2005.01.006

Guzewich, S. D., Lemmon, M., Smith, C. L., Martínez, G., Vicente-Retortillo, Á., Newman, C. E., et al. (2019). Mars Science Laboratory observations of the 2018/Mars year 34 global dust storm. *Geophysical Research Letters*, *46*, 71–79. https://doi.org/10.1029/2018GL080839

Haberle, R. M. (1986). Interannual variability of global dust storms on Mars. *Science*, *234*(4775), 459–461. https://doi.org/10.1126/science.234.4775.459

Haberle, R. M., Clancy, R. T., Forget, F., Smith, M. D., & Zurek, R. W. (2017). *The atmosphere and climate of Mars*. United Kingdom: Cambridge University Press.

Haberle, R. M., Pollack, J. B., Barnes, J. R., Zurek, R. W., Leovy, C. B., Murphy, J. R., et al. (1993). Mars atmospheric dynamics as simulated by the NASA Ames General Circulation Model 1. The zonal-mean circulation. *Journal of Geophysical Research*, *98*(E2), 3093–3123. https://doi.org/10.1029/92JE02946

Ignatiev, N., Grassi, D., Guerlet, S., Vlasov, P., Grigoriev, A., Shakun, A., et al. (2019). Thermal structure and dust clouds during the 2018 dust storm from ACS-TIRVIM onboard ExoMars/TGO, EGU2019-14988.

Kass, D. M., Kleinböhl, A., McCleese, D. J., Schofield, J. T., & Smith, M. D. (2016). Interannual similarity in the Martian atmosphere during the dust storm season. *Geophysical Research Letters*, *43*, 6111–6118. https://doi.org/10.1002/2016GL068978

Malin, M. C., Cantor, B. A., & Britton, A. W. (2018a). MRO MARCI weather report for the week of 21 May 2018–27 May 2018, Malin Space Science Systems Captioned Image Release, MSSS-532. Retrieved from http://www.msss.com/msss_images/2018/05/30/

Malin, M. C., Cantor, B. A., & Britton, A. W. (2018b). MRO MARCI weather report for the week of 28 May 2018–3 June 2018, Malin Space Science Systems Captioned Image Release, MSSS-533. Retrieved from http://www.msss.com/msss_images/2018/06/06/

Malin, M. C., Cantor, B. A., & Britton, A.W. (2018c). MRO MARCI weather report for the week of 4 June 2018–10 June 2018, Malin Space Science Systems Captioned Image Release, MSSS-534. Retrieved from http://www.msss.com/msss_images/2018/06/13/

Malin, M. C., Cantor, B. A., & Britton, A. W. (2018d). MRO MARCI weather report for the week of 11 June 2018–17 June 2018, Malin Space Science Systems Captioned Image Release, MSSS-535. Retrieved from http://www.msss.com/msss_images/2018/06/20/

Malin, M. C., Cantor, B. A., & Britton, A. W. (2018e). MRO MARCI weather report for the week of 18 June 2018–24 June 2018, Malin Space Science Systems Captioned Image Release, MSSS-536. Retrieved from http://www.msss.com/msss_images/2018/06/27/

Malin, M. C., Cantor, B. A., & Britton, A. W. (2018f). MRO MARCI weather report for the week of 2 July 2018–8 July 2018, Malin Space Science Systems Captioned Image Release, MSSS-538. Retrieved from http://www.msss.com/msss_images/2018/07/11/

Malin, M. C., Cantor, B. A., & Britton, A. W. (2018g). MRO MARCI weather report for the week of 16 July 2018–22 July 2018, Malin Space Science Systems Captioned Image Release, MSSS-540. Retrieved from http://www.msss.com/msss_images/2018/07/25/

Montabone, L., Spiga, A., Kass, D. M., Kleinböhl, A., Forget, F., & Millour, E. (2020). Martian Year 34 column dust climatology from Mars Climate Sounder Observations: Reconstructed maps and model simulations. *Journal of Geophysical Research: Planets*, *125*, e2019JE006111. https://doi.org/10.1029/2019JE006111

Murphy, J. R., Toon, O. B., Haberle, R. M., & Pollack, J. B. (1990). Numerical simulations of the decay of Martian global dust storms. *Journal of Geophysical Research*, *95*(B9), 14,629–14,648. https://doi.org/10.1029/JB095iB09p14629

Pankine, A. A. (2015). The nature of the systematic radiometric error in the MGS TES spectra. *Planetary and Space Science*, *109-110*, 64–75. https://doi.org/10.1016/j.pss.2015.01.022

Pankine, A. A. (2016). Radiometric error and re-calibration of the MGS TES spectra. *Planetary and Space Science*, *134*, 112–121. https://doi.org/10.1016/j.pss.2016.10.015

Smith, M. D. (2004). Interannual variability in TES atmospheric observations of Mars during 1999–2003. *Icarus*, *167*(1), 148–165. https://doi.org/10.1016/j.icarus.2003.09.010

Smith, M. D. (2008). Spacecraft observations of the Martian atmosphere. *Annual Review of Earth and Planetary Sciences*, *36*(1), 191–219. https://doi.org/10.1146/annurev.earth.36.031207.124334

Smith, M. D. (2009). THEMIS observations of Mars aerosol optical depth from 2002–2008. *Icarus*, *202*(2), 444–452. https://doi.org/10.1016/j.icarus.2009.03.027

Smith, M. D., Bandfield, J. L., & Christensen, P. R. (2000). Separation of atmospheric and surface spectral features in Mars Global Surveyor Thermal Emission Spectrometer (TES) spectra. *Journal of Geophysical Research*, *105*(E4), 9589–9607. https://doi.org/10.1029/1999JE001105

Smith, M. D., Conrath, B. J., Pearl, J. C., & Christensen, P. R. (2002). Thermal Emission Spectrometer observations of Martian planet-encircling dust storm 2001A. *Icarus*, *157*(1), 259–263. https://doi.org/10.1006/icar.2001.6797

Smith, M. D., Pearl, J. C., Conrath, B. J., & Christensen, P. R. (2000). Mars Global Surveyor Thermal Emission Spectrometer (TES) observations of dust opacity during aerobraking and science phasing. *Journal of Geophysical Research*, *105*(E4), 9539–9552. https://doi.org/10.1029/1999JE001097

Strausberg, M., Wang, H., Richardson, M. I., Ewald, S. P., & Toigo, A. D. (2005). Observations of the initiation and evolution of the 2001 Mars global dust storm. *Journal of Geophysical Research*, *110*, E02006. https://doi.org/10.1029/2004JE002361

Vandaele, A. C., Korablev, O., Daerden, F., Aoki, S., Thomas, I. R., Altieri, F., et al., NOMAD Science Team, & ACS Science Team (2019). Martian dust storm impact on atmospheric $H_2O$ and D/H observed by ExoMars Trace Gas Orbiter. *Nature*, *568*(7753), 521–525. https://doi.org/10.1038/s41586-019-1097-3

Wang, H., & Richardson, M. I. (2015). The origin, evolution, and trajectory of large dust storms on Mars during years 24-30 (1999 – 2011). *Icarus*, *251*, 112–127. https://doi.org/10.1016/j.icarus.2013.10.033

Wilson, R. J., & Richardson, M. I. (2000). The Martian atmosphere during the Viking Mission, I, infrared measurements of atmospheric temperatures revisited. *Icarus*, *145*, 555–579. https://doi.org/10.1006/icar.2000.6378

Wolkenberg, P., Giuranna, M., Grassi, D., Aronica, A., Aoki, S., Scaccabarozzi, D., & Saggin, B. (2018). Characterization of dust activity on Mars from MY27 to MY32 by PFS-MEX observations. *Icarus*, *310*, 32–47. https://doi.org/10.1016/j.icarus.2017.10.045

Wolkenberg, P., Smith, M. D., Formisano, V., & Sindoni, G. (2011). Comparison of PFS and TES observations of temperature and water vapor in the Martian atmosphere. *Icarus*, *215*(2), 628–638. https://doi.org/10.1016/j.icarus.2011.07.032

Wolkenberg, P., Giuranna, M., Smith, M. D., & Grassi, D. (2019). "TES and PFS observations during MY 25, MY 28 and MY 34", Mendeley Data, v1. https://doi.org/10.17632/5s5c8j5g2f.1

Zurek, R. W., Barnes, J. R., Haberle, R. M., Pollack, J. B., Tillman, J. E., & Leovy, C. B. (1992). In H. H. Kieffer, et al. (Eds.), *Dynamics of the atmosphere of Mars* (pp. 835–933). Tucson: University of Arizona Press.